Space Weather

RESEARCH ARTICLE
10.1029/2025SW004843

Special Collection:
The Space Weather Research to Operation to Research (R2O2R) Pipeline(s): Progress, Challenges and Prospects

Validating SCUBAS Predictions of Geomagnetically Induced Voltage in Submarine Cables Using Legacy Superstorm Observations

S. Chakraborty[1], M. D. Hartinger[2,3], X. Shi[4], D. H. Boteler[5,6], E. Lawrence[7], C. Boteler[8], J. B. H. Baker[9], and M. Macalester[10]

[1]Embry-Riddle Aeronautical University, Daytona Beach, FL, USA, [2]Space Science Institute, Boulder, CO, USA, [3]University of California, Los Angeles, CA, USA, [4]Department of Physics and Astronomy, Clemson University, Clemson, SC, USA, [5]Natural Resource Canada, Ottawa, Ontario, Canada, [6]Physics Department, Lancaster University, Lancaster, UK, [7]British Geological Survey, Edinburgh, UK, [8]National Oceanography Centre, Southampton, UK, [9]Bradley Department of Electrical and Computer Engineering, Virginia Tech, Blacksburg, VA, USA, [10]Department of Homeland Security, Cybersecurity and Infrastructure Security Agency, Washington, DC, USA

Abstract Modern submarine communication cables, though fiber-optic in nature, remain vulnerable to space weather hazards due to their internal conductive cables used for powering repeaters. During geomagnetic storms, variations in the geomagnetic field induce geoelectric fields that drive geomagnetically induced voltages along these cables. This study validates the Submarine Cable Upset By Auroral Streams (SCUBAS) model framework by analyzing the induced voltages on two transatlantic submarine cables—TAT-1 and TAT-8—during the 11 February 1958 and 13 March 1989 superstorms, respectively. SCUBAS models the cable as a segmented conductor placed atop oceanic and subsea conductivity structures and calculates voltages from both cable-parallel electric fields and coastal Earth potential at cable terminals. Model outputs are compared against digitized observations from historical literature. SCUBAS successfully captures both large-scale voltage patterns and event-specific dynamics, reproducing peak voltages within a median percentage error of <30%. High skill scores (>0.85) further confirm the reliability of the model across events and spatial locations. The results highlight that both subsea induction and coastal Earth potential shifts contribute significantly to geomagnetically induced voltages, emphasizing the need for comprehensive modeling in space weather risk assessments. This validation positions SCUBAS as a robust tool for evaluating the vulnerability of submarine cables to geomagnetic disturbances, with relevance for space weather forecasting, improving infrastructure resilience, and future mitigation strategies.

Plain Language Summary Submarine internet cables use fiber optics to carry data, but they still rely on long conductive wires to power repeaters on the seafloor. During major space weather events, changes in Earth's magnetic field can induce electrical voltages on these power-feed conductors. This study uses the Submarine Cable Upset By Auroral Streams model to estimate voltages on two transatlantic cables during historic geomagnetic storms in 1958 and 1989. The model closely matches observed voltages and shows that both seafloor induction and coastal electric fields contribute to cable risk. These results help improve assessments of space-weather impacts on global communication infrastructure.

Key Points:

- Study compares Submarine Cable Upset By Auroral Streams (SCUBAS) model predictions against cable voltages recorded during two legacy superstorms of last century
- SCUBAS successfully captures both large-scale voltage patterns and event-specific dynamics
- Overall median percentage error and skill score of SCUBAS are <30% and 0.85 respectively

Supporting Information:

Supporting Information may be found in the online version of this article.

Correspondence to:

S. Chakraborty,
chakras4@erau.edu

Citation:

Chakraborty, S., Hartinger, M. D., Shi, X., Boteler, D. H., Lawrence, E., Boteler, C., et al. (2026). Validating SCUBAS predictions of geomagnetically induced voltage in submarine cables using legacy superstorm observations. *Space Weather*, *24*, e2025SW004843. https://doi.org/10.1029/2025SW004843

Received 19 NOV 2025
Accepted 5 JUN 2026

Author Contributions:

Conceptualization: S. Chakraborty, M. D. Hartinger, X. Shi, D. H. Boteler, J. B. H. Baker, M. Macalester
Data curation: D. H. Boteler, E. Lawrence, C. Boteler
Formal analysis: S. Chakraborty, M. D. Hartinger, X. Shi

1. Introduction

Despite advancements in satellite communication technologies, global internet infrastructure continues to rely heavily on undersea telecommunication pathways, commonly known as submarine cables. These systems remain critical for high-fidelity, high-capacity, and trans-oceanic data transmission (Carter et al., 2009). The early high-capacity submarine cables, developed in the 1950s, were coaxial and constructed entirely from metallic conductors (Ash, 2016). As such, they were susceptible to geomagnetically induced voltages during geomagnetic storm events. With the introduction of fiber-optic technology in the early 1980s, these older metallic cables were gradually phased out and replaced. While fiber optics themselves are not susceptible to geomagnetic induction, the accompanying power-feed lines—which deliver electricity to underwater repeaters and other equipment—are still made of conductive metals. Consequently, modern fiber-optic systems remain vulnerable to space weather through these long conducting metallic wires, particularly during geomagnetic superstorms (e.g., Boteler, 2019; Boteler et al., 2024; Lanzerotti, 2007, 2017; Lanzerotti et al., 2001). Since disruption to these cables can impact

Funding acquisition: S. Chakraborty, M. D. Hartinger, X. Shi
Investigation: S. Chakraborty, X. Shi, D. H. Boteler
Methodology: S. Chakraborty
Project administration: S. Chakraborty
Resources: E. Lawrence, C. Boteler
Software: S. Chakraborty
Validation: D. H. Boteler
Writing – original draft: S. Chakraborty, M. D. Hartinger
Writing – review & editing: M. D. Hartinger, X. Shi, D. H. Boteler, C. Boteler, J. B. H. Baker, M. Macalester

international communication, ensuring the security and resilience of submarine cables is paramount (e.g., Barlow, 1849; McManus et al., 2011). The most significant past disruption was recorded during the solar eruptions of August/September 1859 (Prescott, 1866). Additionally, in the recent past the March 1989 and February 1958 geomagnetic storms created impacts on modern critical infrastructure leading to economic impact. These solar eruptions led to the largest geomagnetic disturbances (GMD) of modern times (NERC, 2022), which caused widespread disruptions in the underwater telegraph and cable systems (Boteler, 2006).

We have developed a modeling capability to quantify geomagnetic induction effects and their downstream impacts on submarine cable operations—specifically, electrical voltage surges induced during space weather events. This model, called Submarine Cable Upset By Auroral Streams (SCUBAS; Chakraborty et al., 2022), has been applied in several previous studies examining the voltages induced in the submarine cables during geomagnetically disturbed periods (e.g., Boteler et al., 2024). A detailed methodology and description of the computational modules of the SCUBAS model are presented in Chakraborty et al. (2022).

A significant challenge in validating SCUBAS arises from the limited availability of submarine cable voltage data sets, which are often restricted due to proprietary information and security concerns. It is important to note that SCUBAS is not intended to replace more computationally intensive three-dimensional electromagnetic models that resolve detailed induction physics. Rather, it is designed as a practical and scalable framework for estimating induced voltages and currents in submarine cable systems, consistent with applications in industry and operational risk assessment. Nevertheless, in this study, we perform data-model validation by comparing SCUBAS output to observations reported in prior literature. Our focus centers on two major geomagnetic superstorms: the 11 February 1958 and 13 March 1989 events, both characterized by D_{st} values below −400 nT. During the February 1958 storm, the TAT-1 coaxial transatlantic cable experienced substantial signal disruptions. Telephone calls were affected by alternating loud squawks and faint whispers, attributed to the interference between geomagnetically induced voltages and the cable's power supply (Anderson, 1978; Anderson et al., 1974). The March 1989 storm further exposed this vulnerability. Although the TAT-8 cable employed modern fiber-optic transmission, it still experienced voltage surges of up to 700 V induced on its metallic power-feed lines. While no operational disruptions occurred, the voltage regulation was pushed to its limits, highlighting that such space-weather-driven effects remain a continuing concern (Medford et al., 1989).

Validating SCUBAS predictions during these historical case studies is a crucial step in establishing it as a reliable first-principle tool for assessing submarine cable vulnerability to GMD. In this study, we focus on a ∼24-hr time interval (in two different blocks) for the 1989 storm and ∼4-hr interval for the 1958 storm due to the limited availability of reliable historical voltage data.

2. Model Setup

2.1. Model: SCUBAS

In this study, SCUBAS is used to estimate storm-time voltages along the TAT-1 and TAT-8 transatlantic cables by coupling observed geomagnetic variations to a physics-based electromagnetic induction framework. The model links surface magnetic field perturbations to seafloor electric fields through a frequency-dependent transfer function derived from a 1-D layered Ocean–Earth conductivity structure. This formulation accounts for the shielding effect of seawater, as well as the dispersive response of the underlying lithosphere, allowing different temporal scales of geomagnetic effects to produce distinct induced electric field signatures. A detailed description and validation of the SCUBAS framework are given in Chakraborty et al. (2022) and Boteler et al. (2023), where the model formulation and its application to submarine cable systems are presented. Here we provide only a brief summary of the key components relevant to this study and refer the reader to these works for full details.

The computed geoelectric field (GEF) is projected along the actual cable route, which is discretized into sections consistent with bathymetry and electrical properties. The choice of the section is manual and primarily depends on comparable water depth and length of the segments. For each section, the induced electric field generates an electromotive force (EMF), which is integrated along the cable length. In parallel, SCUBAS evaluates cross-ocean electric voltages and the associated Earth potentials at the cable landing points using distributed-source transmission line (DSTL) theory. This step ensures that both along-cable induction and boundary-driven potential differences contribute to the final voltage estimate.

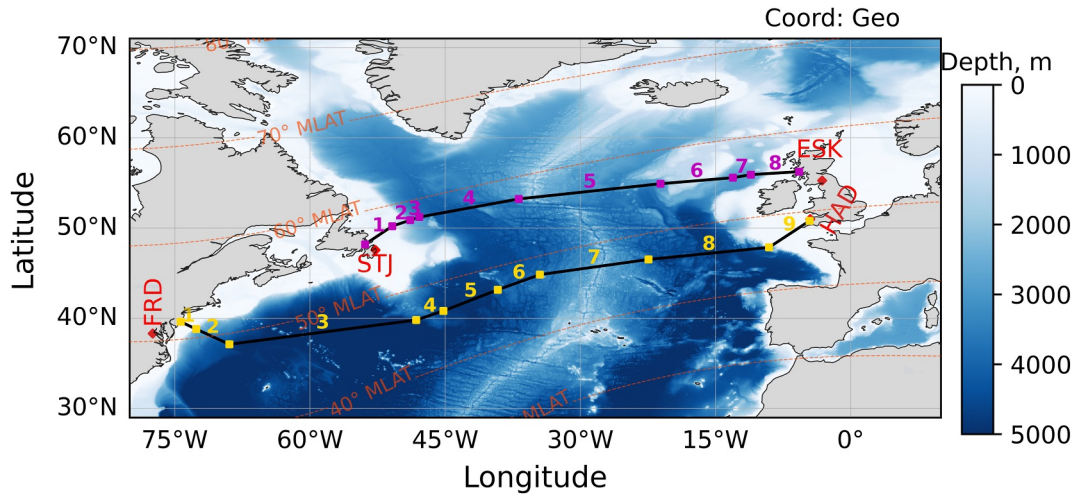

Figure 1. Route of the TAT-1 (black line with magenta squares) and TAT-8 (black line with yellow squares) submarine cables across the Atlantic. The numbers in magenta and yellow correspond to the cable sections described in Tables 1 and 2, respectively. Red diamonds show locations of the Fredericksburg (FRD), St Johns (STJ), Hartland (HAD), and Eskdalemuir (ESK) magnetic observatories. Red dotted curves indicate magnetic latitude contours.

The total voltage is obtained by combining the calculated EMF along the cable with the difference in Earth potential at its ends. For long cables such as TAT-1 (~4,000 km) and TAT-8 (~8,000 km), the model effectively links storm-scale magnetic variability to spatially distributed induction along the cable route. The approach is most reliable when the driving magnetic disturbances are coherent over scales comparable to the cable length and when lateral conductivity contrasts are small relative to vertical changes. Where current systems are highly structured or magnetometer coverage is sparse, the resulting voltage estimates should be interpreted as large-scale approximations rather than fully resolved local responses.

2.2. Model Geometry

This section outlines the geographic configuration of the TAT-1 and TAT-8 transatlantic submarine cables, their segmentation based on ocean bathymetry, and the assignment of nearby magnetic observatories to specific cable segments for geomagnetic analysis.

Figure 1 illustrates the routes of the TAT-1 and TAT-8 cables. TAT-1 is represented by black line segments marked with magenta squares, while TAT-8 is shown as black segments with gold squares. The TAT-1 cable spanned approximately 3,900 km, connecting Clarenville, Newfoundland to Oban, Scotland. The TAT-8 cable extended about 6,300 km from Tuckerton, New Jersey, to a branching point off the French coast (not shown in this Figure), where it connects to Widemouth Bay, UK (50.79°N, 4.55°W), and Penmarch, France (47.8°N, 4.34°W), as described in Figure 4a of Boteler et al. (2024). For simplicity, the SCUBAS model uses the start and end points of the main trunk of each cable to define simulation boundaries. The TAT-8 system was powered by constant voltage sources at the UK and French ends and a constant current feed at Tuckerton. Voltage fluctuations induced by GMD were monitored at Tuckerton by observing changes in the power feed equipment, enabling empirical measurements of induced voltages (Medford et al., 1989). Bathymetry of the Atlantic Ocean is depicted using a color-coded scale at the side of the figure. The locations of nearby magnetic observatories—Fredericksburg (FRD), St. John's (STJ), Hartland (HAD), and Eskdalemuir (ESK)—are indicated by black diamonds. These observatories were assigned to the closest corresponding cable segments to provide magnetic field inputs for the SCUBAS model.

Figures 2a and 2b displays the bathymetric profiles of the TAT-1 and TAT-8 cables, respectively, along their transatlantic routes. These plots illustrate how the cables were segmented for modeling purposes based on changes in seafloor depth. Following the methodology described by Boteler et al. (2024), we do not compute the induced electric fields by accounting for every detailed variation in seabed topography. Instead, we approximate the ocean floor as a series of discrete, flat segments, represented by black step-like profiles in Figure 2. This segmented approach simplifies the modeling of seafloor conductivity structures while preserving the overall

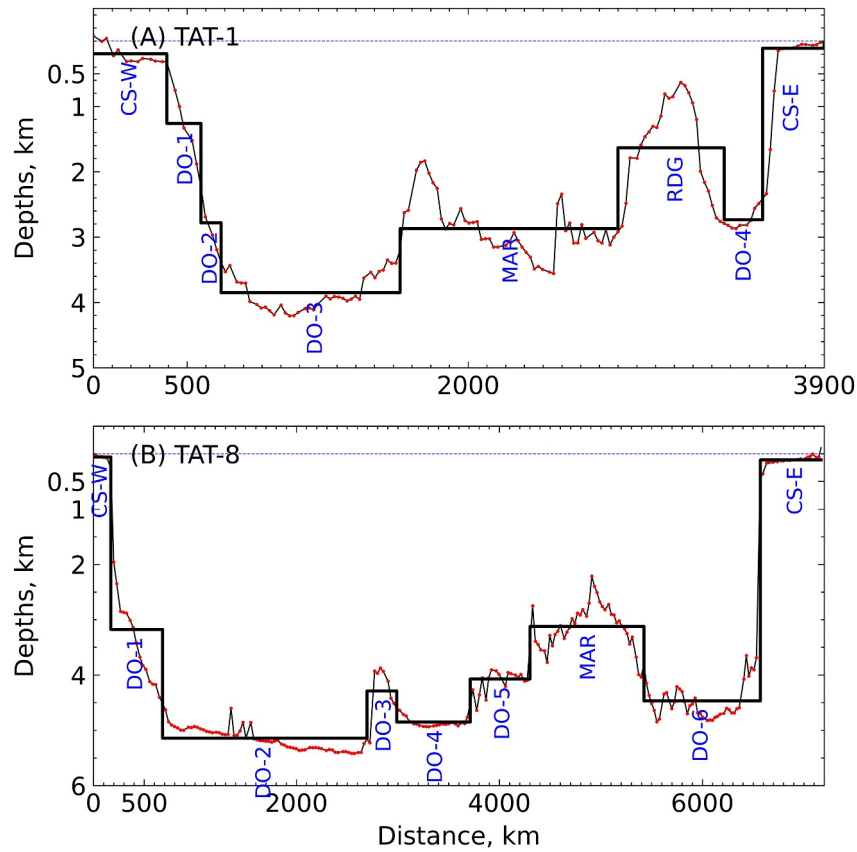

Figure 2. Depth profile of the (a) TAT-1, and (b) TAT-8 cable routes. Black blocks (with blue annotations) show the approximation of the seafloor by flat sections used in the electric field calculations. Note that CS, DO, MAR, and RDG stand for Continental Shelf, Deep Ocean, Mid Atlantic Ridge, and Ridge. W and E indicate west and east edge of the cables.

bathymetric trend. The boundaries of each segment are indicated by magenta squares (TAT-1) and yellow square (TAT-8), corresponding to the cable section markers shown in Figure 1. This approach enables a practical and computationally efficient framework inside SCUBAS for estimating electric fields and voltages induced along the cable during GMD.

To calculate the induced electric fields, the SCUBAS model requires three primary inputs: (a) the detailed submarine cable routes (previously described), (b) time-varying geomagnetic field measurements along those routes, and (c) one-dimensional ocean–Earth conductivity profiles for each cable segment. A key limitation in this modeling effort is the absence of direct magnetic field measurements over oceanic regions. To overcome this, we rely on land-based magnetic observatories situated near the endpoints of the cables. An additional challenge stems from the historical nature of the geomagnetic events under study (1958 and 1989). Many magnetic observatories currently in operation were not active during those years. Furthermore, most observatories operational during the 1958 storm used analog methods to measure the geomagnetic field, with daily variations captured on a paper magnetogram often with unknown scale and temporal resolution (Beggan et al., 2024). In several cases, the magnetograms for the periods of interest were either missing or unreadable, further restricting data availability. Despite these constraints—stemming from both technological limitations and sparse spatial coverage—we were able to obtain and digitize the necessary magnetic data during the 1958 storm with the assistance of the British Geological Survey (BGS) and the United States Geological Survey (USGS). For the TAT-1 cable, we used geomagnetic data from the Eskdalemuir (ESK) observatory for all the cable sections. In an ideal case the St. John's (STJ) observatory is geographically closer to the western edge of TAT-1 cable and should be used for modeling. However, due to limitations in data availability from the St. John's observatory in 1958, we utilized magnetic field measurements from Eskdalemuir assuming the ionospheric current structure is constant for the whole cable length of 4,000 km. For the TAT-8 cable during March 1989 storm, we used FRD and HAD, and we also included

Table 1
Location and Characteristics of the Cable Sections of TAT-1 Cable Route That Are Shown in Figure 1 (in Magenta), Along With the Earth Model and Magnetic Observatory Used in SCUBAS to Compute Total Induced Voltage

Section	Western edge	Eastern edge	Depth (km)	Earth model	Magnetic observatory
1	48.19°N,53.88°W	50.20°N,50.87°W	0.27	$CS\text{-}W_1$	ESK
2	50.20°N,50.87°W	50.87°N,48.87°W	1.33	$DO\text{-}1_1$	ESK
3	50.87°N,48.87°W	51.21°N,47.86°W	2.83	$DO\text{-}2_1$	ESK
4	51.21°N,47.86°W	53.22°N,36.82°W	3.94	$DO\text{-}3_1$	ESK
5	53.22°N,36.82°W	54.90°N,21.10°W	2.93	MAR_1	ESK
6	54.90°N,21.10°W	55.57°N,13.07°W	1.43	RDG_1	ESK
7	55.57°N,13.07°W	55.91°N,11.06°W	2.81	$DO\text{-}4_1$	ESK
8	55.91°N,11.06°W	56.24°N,5.71°W	0.11	$CS\text{-}E_1$	ESK

Note. Note that CS, DO, MAR, and RDG stand for Continental Shelf, Deep Ocean, Mid Atlantic Ridge, and Ridge. W and E indicate west and east edge of the cables.

additional midsection coverage using data from the St. Johns (STJ) observatory in Newfoundland, located north of the cable route (see Figure 1). The allocation of observatories to specific cable segments was based on geographic proximity to the segment midpoints and is detailed in Tables 1 and 2. This approach ensures the best available representation of geomagnetic variations across each segment for SCUBAS modeling.

2.3. Transfer Functions Along the Cable Routes

To calculate the electric fields induced at the seafloor by geomagnetic field fluctuations, SCUBAS requires knowledge of the electromagnetic transfer function linking horizontal magnetic field variations at Earth's surface to the horizontal electric fields at the seafloor along each cable segment (Boteler et al., 2023). This transfer function is highly sensitive to both the ocean depth and conductivity, as well as the subsurface impedance structure beneath the seabed (Boteler et al., 2023).

Although both the TAT-1 and TAT-8 cables cross the Atlantic Ocean and traverse similar geological settings, there are important differences in their latitudinal placement and seafloor topography. Notably, TAT-1 lies at a higher latitude, and it has a cable route that is associated with greater bathymetric variability and potentially lower water shielding effects on electric field induction (Boteler et al., 2024). To address lateral conductivity variations along the cable routes, we adopt a segmented approach in which different one-dimensional (1-D) conductivity models are applied to distinct geophysical zones, as recommended by Marti et al. (2014). This piecewise

Table 2
Location and Characteristics of the Cable Sections of TAT-8 Cable Route That Are Shown in Figure 1 (in Yellow), Along With the Earth Model and Magnetic Observatory Used in SCUBAS to Compute Total Induced Voltage (Adopted From Boteler et al., 2024)

Section	Western edge	Eastern edge	Depth (km)	Earth model	Magnetic observatory
1	39.60°N,74.33°W	38.79°N,72.62°W	0.1	$CS\text{-}W_8$	FRD
2	38.79°N,72.62°W	37.11°N,68.94°W	4.0	$DO\text{-}1_8$	FRD
3	37.11°N,68.94°W	39.80°N,48.20°W	5.2	$DO\text{-}2_8$	STJ
4	39.80°N,48.20°W	40.81°N,45.19°W	4.0	$DO\text{-}3_8$	STJ
5	40.81°N,45.19°W	43.15°N,39.16°W	4.8	$DO\text{-}4_8$	STJ
6	43.15°N,39.16°W	44.83°N,34.48°W	4.0	$DO\text{-}5_8$	STJ
7	44.83°N,34.48°W	46.51°N,22.43°W	3.0	MAR_8	STJ
8	46.51°N,22.43°W	47.85°N,9.05°W	4.5	$DO\text{-}6_8$	HAD
9	47.85°N,9.05°W	50.79°N,4.55°W	0.1	$CS\text{-}E_8$	HAD

Note. Note that CS, DO and MAR stand for Continental Shelf, Deep Ocean and Mid Atlantic Ridge. W and E indicate west and east edge of the cables.

Table 3
Seawater Depths and 1-D Subsea Earth Conductivity Models for the Sections of the TAT-1 Submarine Cable Route That Are Shown in Figure 1

Layers	ρ_0, Ω-m	Thickness (km)							
		CS-W$_1$	DO-1$_1$	DO-2$_1$	DO-3$_1$	MAR$_1$	RDG	DO-4$_1$	CS-E$_1$
Seawater	0.3	0.27	1.33	2.83	3.94	2.93	1.43	2.81	0.11
Sediments	3	2.1	5.4	2.9	0.98	0.76	1.4	2.9	1
Crust	3000	36	13.5	13	10.3	13.3	22.8	15.7	27.3
Lithosphere	1000	154.5	64.5	73	77.6	39	59.4	41	39.2
Upper Mantle	100	217	325	318	317.5	353.8	324.5	347.6	341.8
Transition Zone	10	250	250	250	250	250	250	250	250
Lower Mantle	1	340	340	340	340	340	340	340	340

modeling strategy allows us to capture local variations in ocean and crustal structure without requiring full three-dimensional modeling. Within each segment, electromagnetic induction is treated using a vertically stratified (1-D) conductivity structure, consistent with the thin-wire approximation underlying DSTL theory. In this framework, the conductivity structure within each segment is represented using a thin-sheet approximation in which electrical properties vary only with depth (1-D stratification), while lateral changes are introduced discretely between segments along the cable route. This assumes that the cable length greatly exceeds its cross-sectional scale and that induction is dominated by vertical impedance structure and along-cable electric fields, rather than by transverse two-dimensional conductivity gradients. Seafloor depths along the cable paths are extracted from the ETOPO1 global relief model (Amante & Eakins, 2009), while subsurface Earth conductivity profiles are based on the LITHO1.0 global reference model (Pasyanos et al., 2014). These inputs are summarized in Tables 3 and 4. In general, the cables traverse shallow continental shelf (CS) regions at both termini, with intermediate segments spanning deep ocean (DO) environments. The Mid-Atlantic Ridge, an elevated seabed structure characterized by greater upper mantle thickness due to magmatic upwelling, is treated as a distinct region to account for its anomalous properties.

The segmented 1-D framework resolves large-scale voltage variations and induction patterns driven by magnetic perturbations coherent over hundreds to thousands of kilometers. However, it does not explicitly resolve transverse two-dimensional conductivity gradients or localized edge effects that may arise from abrupt bathymetric transitions. Increasing the number of segments improves representation of along-route variability, but segmentation below scales of a few hundred kilometers begins to challenge the thin-wire assumption inherent to the DSTL formulation, which requires lateral gradients along the cable to dominate over cross-sectional structure. Thus, model fidelity reflects a balance between spatial resolution and consistency with the underlying electromagnetic approximations.

Table 4
Seawater Depths and 1-D Subsea Earth Conductivity Models for the Sections of the TAT-8 Submarine Cable Route That Are Shown in Figure 1

Layers	ρ_0, Ω-m	Thickness (km)								
		CS-W$_8$	DO-1$_8$	DO-2$_8$	DO-3$_8$	DO-4$_8$	DO-5$_8$	MAR$_8$	DO-6$_8$	CS-E$_8$
Seawater	0.3	0.1	4	5.2	4	4.8	4	3	4.5	0.1
Sediments	3	8	4	2	2	1	0.5	0	1.5	3
Crust	3000	15	10	10	10	10	10	10	10	20
Lithosphere	1000	150	145	140	140	70	60	25	70	120
Upper Mantle	100	236.9	247	252.8	254	324.2	335.5	372	324	266.9
Transition Zone	10	250	250	250	250	250	250	250	250	250
Lower Mantle	1	340	340	340	340	340	340	340	340	340

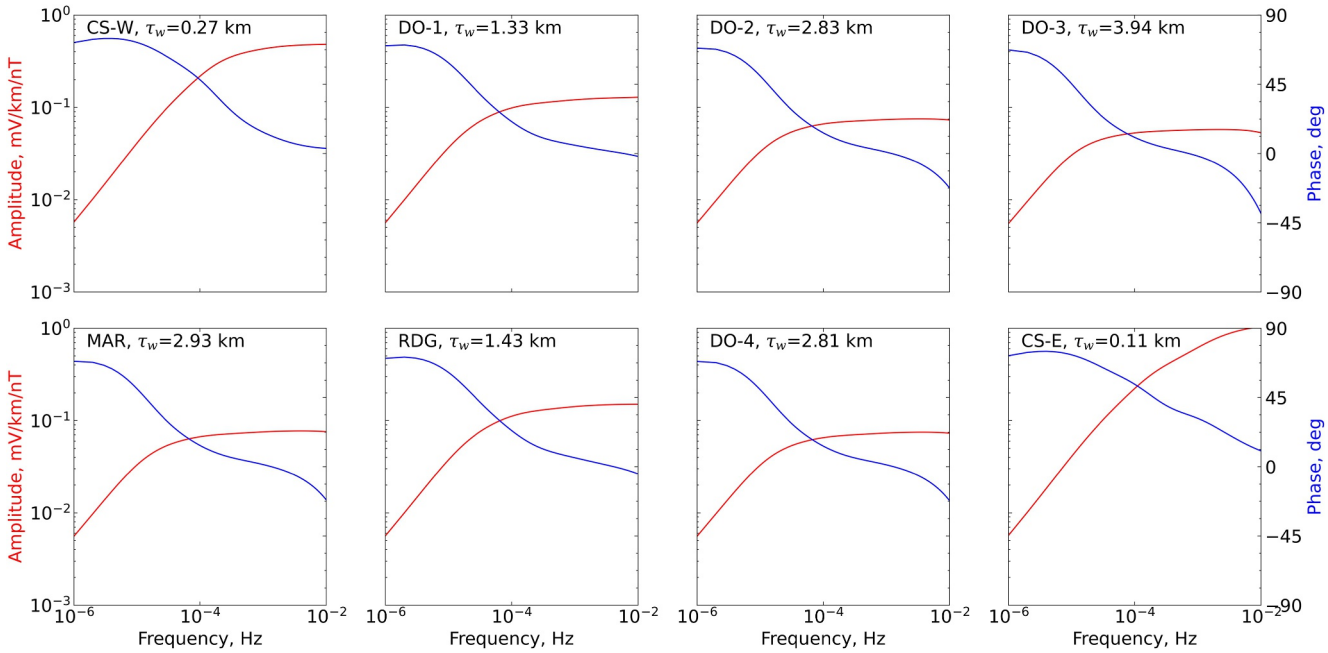

Figure 3. Transfer functions relating the seafloor electric field to the surface magnetic field along TAT-1 cable routes/segments, calculated using the subsea earth models shown in Table 3.

For each segment we derive the electromagnetic transfer function T_x, which relates surface magnetic field variations to induced horizontal electric fields at the seafloor. We employ the methodology outlined by Boteler et al. (2023, 2024), which incorporates seawater depth d and assuming a uniform seawater conductivity ($\sigma_0 = 3$ S/m) (Chakraborty et al., 2022). The Earth conductivity models detailed in Tables 3 and 4 serve as the basis for estimating the seafloor impedance across individual segments of the TAT-1 and TAT-8 cable routes.

Figures 3 and 4 illustrate the resulting transfer functions along the cable segments. A consistent trend emerges: the amplitude of the transfer function diminishes with increasing water depth. This behavior reflects the attenuating effect of deeper seawater layers, which act to shield the seabed from electromagnetic fluctuations. As a result, induced electric fields are substantially weaker in deep-ocean segments compared to those on the shallower CS, highlighting the critical role of bathymetry in shaping submarine cable exposure to geomagnetically induced electric fields. The blue curves in Figures 3 and 4 represent the frequency-dependent phase of the transfer functions. This phase describes the relative timing between magnetic field perturbations and the induced GEF (and consequently geomagnetically induced currents (GIC) response). Its variation reflects the dispersive nature of the layered conductivity structure. We find that the phase behavior depends on water depth: for shallower water, the phase remains largely positive over the frequency range considered, whereas for greater water depth a transition occurs, lower frequencies tend to retain a positive phase, while higher frequencies shift toward negative values. For some of the transfer functions, a narrow intermediate band shows minimal phase variation (near 0^o), suggesting a frequency range where the induced response is nearly in phase with the driving magnetic perturbation.

3. Data Digitization Process

Reconstruction and digitization of historical data constitute a foundational component of this study, as the SCUBAS model relies heavily on magnetometer measurements from February 1958, an event that predates the availability of continuous digital magnetic field observations.

For the March 1989 event, digital magnetometer data sets were readily obtained from the Open Data Resources archive associated with recent work by Boteler et al. (2024). In contrast, for the February 1958 superstorm, we sourced analog magnetograms archived at national observatories. Specifically, the BGS supplied the Eskdalemuir

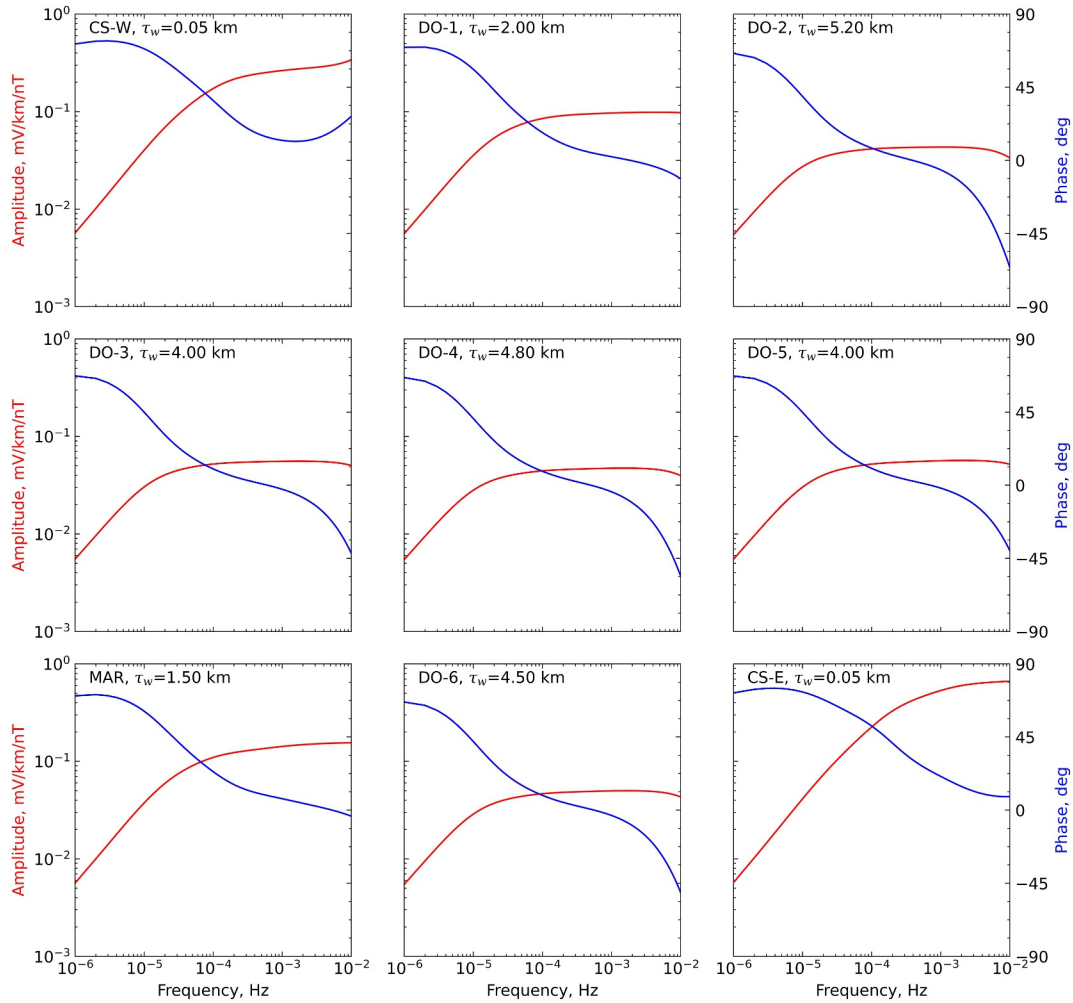

Figure 4. Transfer functions relating the seafloor electric field to the surface magnetic field along TAT-8 cable routes/segments, calculated using the subsea earth models shown in Table 4.

(ESK) records. The BGS further assisted in digitizing these analog data sets to extract the necessary magnetic field components (*H*, *D*, *Z*) used as inputs for SCUBAS model runs.

For validation of SCUBAS model outputs, historical voltage observations from submarine cables were extracted from peer-reviewed literature. The TAT-1 cable voltage during the February 1958 storm was taken from Figure 6 of Axe (1968), and TAT-8 cable voltages during the March 1989 event were obtained from Figures 2 and 3 of Medford et al. (1989). Since these data sets were originally presented as printed figures, a web-based digitization utility was employed to extract the time series data (Rohatgi, n.d.). The tool applied computer vision algorithms to identify and extract data curves, using noise-reduction filters and curve-following techniques. Manual intervention was performed at critical steps to adjust parameters, refine curve detection, and ensure best possible extraction accuracy.

To promote transparency and community reuse, all original magnetogram scans and the historical voltage figures have been archived in a publicly accessible Zenodo repository, which is linked in the Open Science section of this study. The repository also contains detailed documentation of the digitization workflow, including scripts, processing steps, and post-processing corrections, enabling reproducibility and collaborative improvement for future studies involving historical analog data sets. Please refer to Figures S1–S3 in Supporting Information S1 to check the digitized data sets overlaid on top of the original magnetograms.

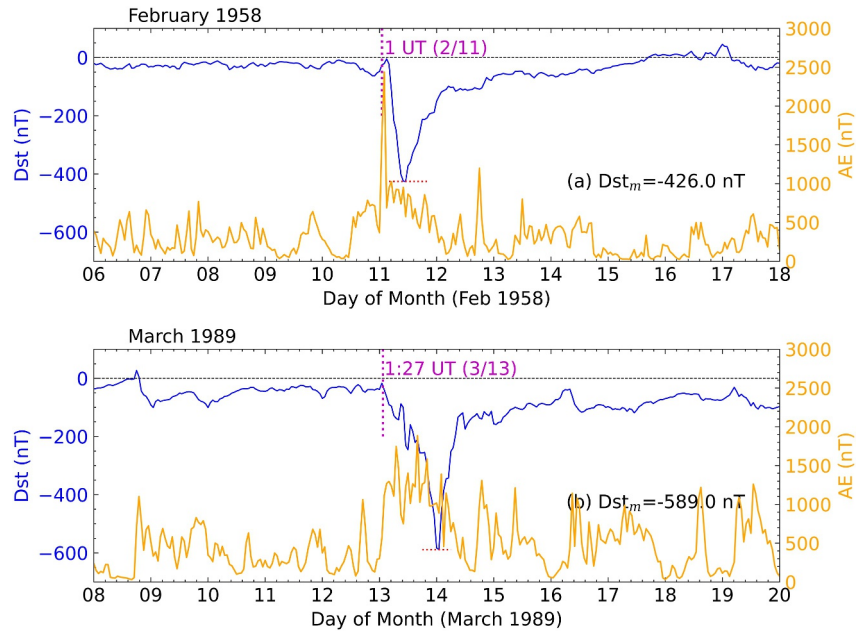

Figure 5. Geomagnetic conditions of the geospace environment depicted by the D_{st} (blue) and AE (yellow) indices during (a) 06–18 February 1958; and (b) 08–20 March 1989. The minimum D_{st} in nT is noted in each panel and indicated by the horizontal dotted magenta line. The storm sudden commencement time is indicated by the vertical dotted magenta line.

4. Event Description

This section describes the geospace conditions associated with the February 1958 and March 1989 geomagnetic storms, focusing on key space weather indices. Figure 5 illustrates the evolution of the geomagnetic environment during each event, represented by the D_{st} and AE indices. In each panel, the minimum D_{st} value is annotated and highlighted by a horizontal magenta dashed line, providing a reference for storm intensity. The vertical magenta dashed line marks the onset of the storm's sudden commencement, indicating the start of the geomagnetic storm. The D_{st} index provides context for the severity and temporal progression of the GMD that influenced the submarine cable systems analyzed in this study. In this study, the D_{st} index is used solely to provide storm-scale context and to indicate the overall intensity of geomagnetic activity. We do not treat D_{st} as a proxy for local GEFs or GICs, as several studies have noted that global indices are often inadequate for detailed GIC assessment due to their limited sensitivity to regional conductivity structure and localized magnetic variability (e.g., Cid et al., 2014; Gil et al., 2021). Direct or modeled GEFs remain more physically meaningful quantities for evaluating GIC impacts.

Solar Cycle 19, which peaked around the time of the International Geophysical Year (IGY: 1957–1958) was one of the strongest solar cycles over the last four centuries and significantly disrupted the solar-terrestrial environment with several solar eruptions and resultant geomagnetic storms (e.g., Hayakawa et al., 2023; Ohtani et al., 2024). The geomagnetic storm of 10–12 February 1958 was triggered by a powerful solar flare and associated ejecta on February 9. Shortly after the flare onset, major radio bursts were detected. Global GMD began around 01:26 UT on February 11, marked by sharp deviations in the horizontal magnetic field 100 nT and intense fluctuations at Fairbanks (e.g., Akasofu & Chapman, 1963). The storm reached maximum intensity, with the D_{st} index plummeting to −426 nT (see Figure 5a). This value indicates a major enhancement of the ring current, consistent with severe geomagnetic activity. Unusually intense auroral displays extended to low latitudes, with red auroras reported across North America, including Cuba and even near 18° magnetic latitude (MLAT) (Kataoka & Kazama, 2019). Eyewitness sketches and a rare Japanese watercolor painted at the time enabled researchers to estimate the auroral altitude (~400 km) and geographic extent (reaching ~41° MLAT), providing a unique view of storm-time ionospheric dynamics (e.g., Kataoka & Kazama, 2019; Kataoka et al., 2019). The February 1958 magnetic storm stands out not only for its striking auroral displays observed well beyond the Arctic but also for its significance in advancing our understanding of space weather phenomena (Ohtani et al., 2024). Figure 6a presents the horizontal geomagnetic field components recorded by the Eskdalemuir magnetometer during the February 1958 storm. Ideally, the St. John's (STJ) observatory, located at the western edge of the TAT-

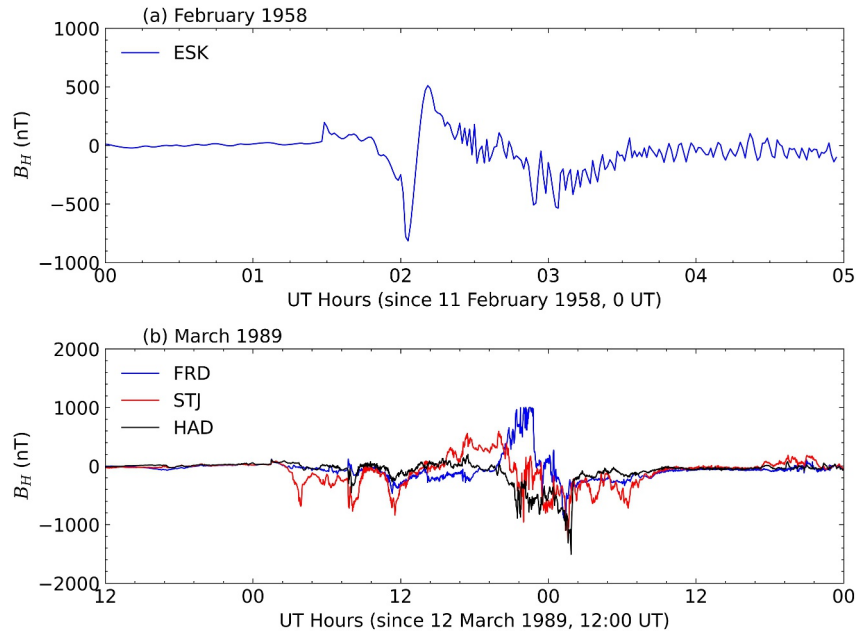

Figure 6. Measured horizontal magnetic field variations ($B_H = \sqrt{B_x^2 + B_y^2}$) during (a) February 1958 storm at Eskdalemuir (ESK) station; and (b) March 1989 storm at Fredericksberg (FRD), St John's (STJ) and Hartland (HAD) stations. These data sets are used in Submarine Cable Upset By Auroral Streams simulations.

1 cable, would have provided a more accurate characterization of the geomagnetic field variations influencing the system. However, due to limitations in data availability and the operational status of observatories during that historical period, magnetic field measurements from Eskdalemuir were used for all cable segments. While this substitution may not fully capture the actual ionospheric current signatures on the event day, it represents the most practical approach given the data constraints.

The 13 March 1989, magnetic storm, one of the strongest in the 20th century, caused widespread power grid disruptions, including a major blackout of the Hydro-Québec system (Boteler, 2019). Figure 6b displays the horizontal geomagnetic field components recorded by ground-based magnetometers during the March 1989 storm. The event was triggered by two coronal mass ejections (CMEs) associated with solar flares on March 10 (X4.5) and March 12 (M7.3). These CMEs produced shock arrivals to Earth at 01:27 and 07:43 UT on March 13. The estimated transit speeds were ∼760 km/s and ∼1320 km/s, respectively. Empirical modeling suggests solar wind speeds peaked near 980 km/s with a southward IMF (Bs) of 40–60 nT (Boteler, 2019). While the D_{st} index reached a record low of −589 nT later in the event, the Hydro-Québec blackout occurred earlier, indicating that severe impacts could precede the D_{st} minimum. Auroral expansion during the storm further caused power issues across the United States, United Kingdom, and Sweden (Boteler, 2019).

5. Simulation Outputs and Data-Model Comparison

This section presents a comparison between observed and SCUBAS-simulated submarine cable voltages during the two geomagnetic storms. Figure 7 illustrates the induced seafloor electric fields along cable segments computed from geomagnetic observatory data and Earth conductivity models (Tables 3 and 4). The left and right columns present simulated seafloor electric fields along the cable segments. Key findings include: (a) the east–west (y) components were significantly stronger than the north–south (x) components for both storms; (b) electric field fluctuations during the 1958 storm were approximately four times greater than those during the 1989 event; and (c) the March 1989 fluctuations were especially pronounced over the CS regions (CS-E_8, CS-W_8), indicating reduced EM shielding due to shallow ocean (Boteler et al., 2023).

Note that the model captures shielding effects through the conductance of DO sections, which attenuate higher-frequency fields and reduce induced voltages relative to shallow shelf regions. Finally, the relative magnitudes of E_x and E_y arise from the induction relationship between horizontal magnetic perturbations and the cable

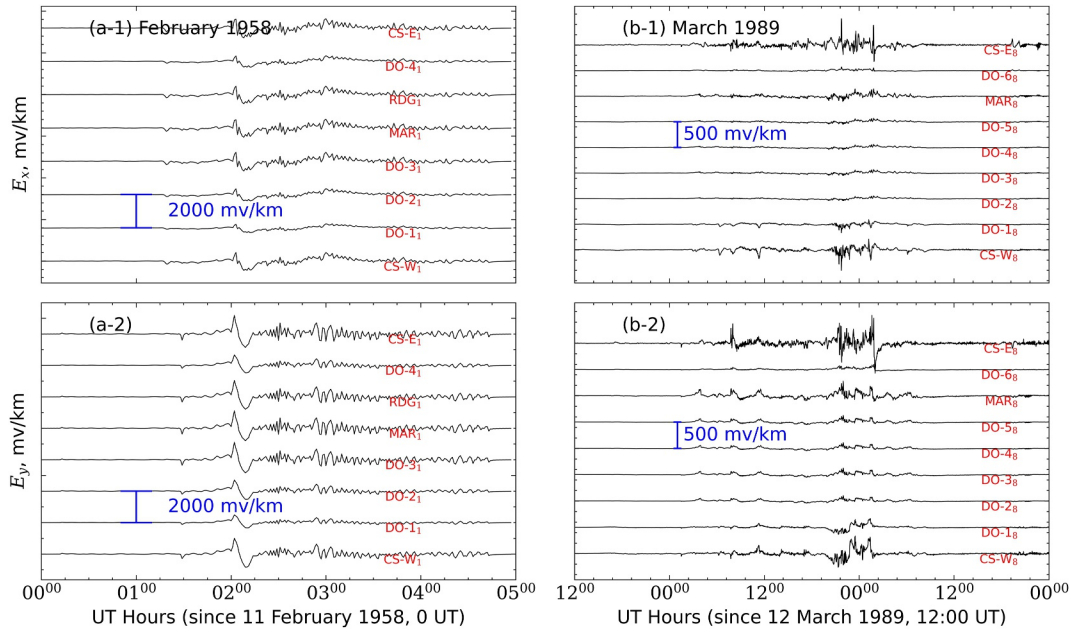

Figure 7. Seafloor electric fields during the magnetic storm of (a-1, a-2) February 1958 calculated for the 8 sections of the TAT-1 cable route across the North Atlantic using the magnetic observatory data and earth models as noted in Table 3, and (b-1, b-2) March 1989 calculated for the 9 sections of the TAT-8 cable route across the North Atlantic using the magnetic observatory data and earth models as noted in Table 4.

orientation. For an east-west cable, variations in B_y preferentially drive E_x (and vice versa), so differences between E_x and E_y reflect both the polarization of the geomagnetic disturbance and the geometric alignment of the cable relative to the coastline and bathymetry. While the thin-sheet formulation does not explicitly resolve fully two-dimensional cross-track current systems, it captures the dominant along-track conductivity contrasts and large-scale induction physics that control the voltage response.

For the February 1958 geomagnetic superstorm, we present a quantitative comparison between SCUBAS model outputs and the measured voltage fluctuations on the TAT-1 submarine cable (Figure 8). The measured voltage data were extracted from historical records published by Winckler et al. (1959) and Axe (1968). A combination of machine learning–assisted digitization and manual correction was employed to ensure the highest possible fidelity in reconstructing these historical data sets, as mentioned in earlier section (Data Digitization Process). The figure displays a 3.5-hr segment of data–model comparison during the early phase of the storm. Due to limitations

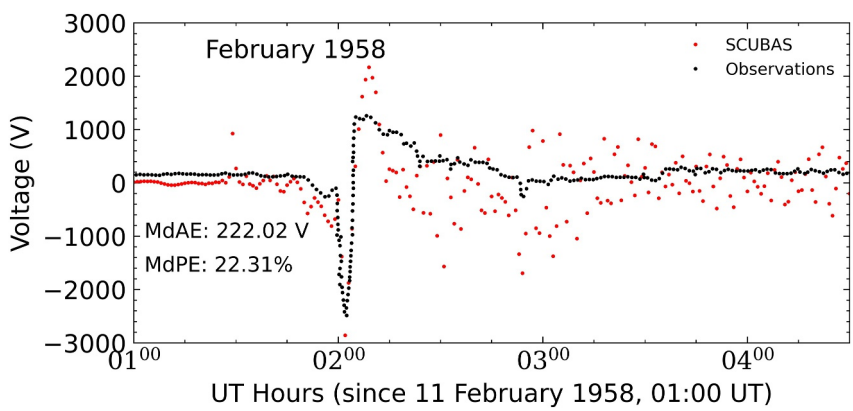

Figure 8. Data-model comparison between observed and modeled voltages along TAT-1 cable during the initial phase of the February 1958 storm between 1:00–4:30 UT on 11th February. Measures of accuracy, the median prediction error (median percentage error) and median absolute error are noted in the figure.

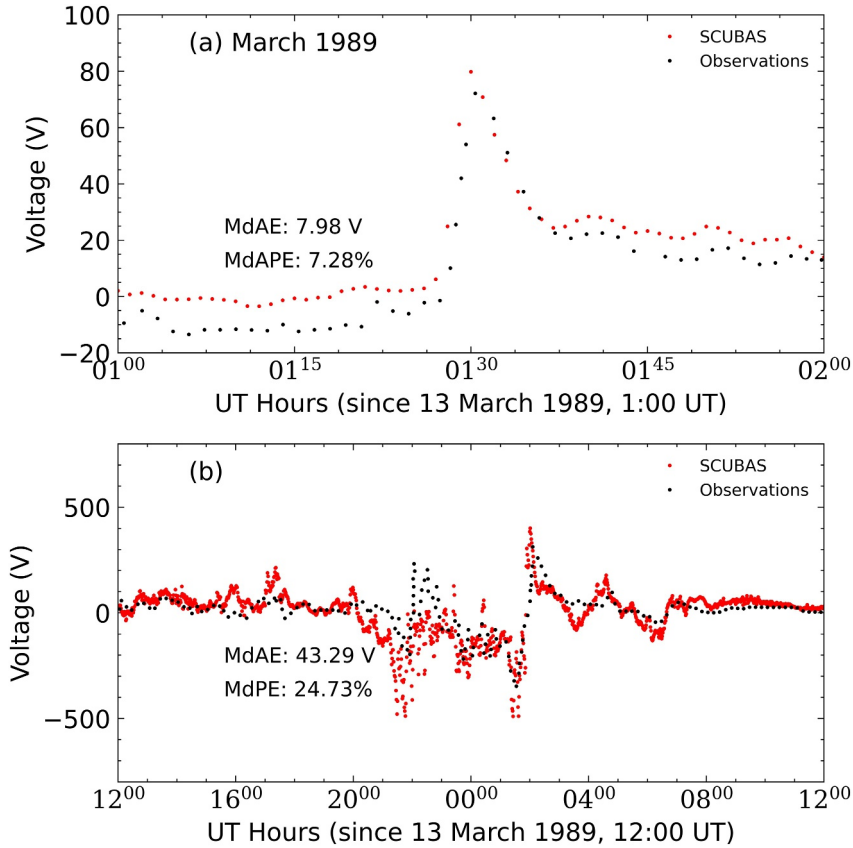

Figure 9. Data-model comparison between observed and modeled voltages along the TAT-8 cable during (a) IP Shock associated with the March 1989 storm during 1:30 UT on 13th March; and (b) the main phase of the March 1989 storm between 12:00 UT on 13th to 12:00 UT on 14th March. The median prediction error is mentioned in each panel.

in the temporal coverage of the published records, the validation is restricted to this interval. We report two summary diagnostics for each comparison window. The median prediction error (MdPE), defined as $\text{MdPE} = \text{median}\left(\frac{V_{\text{SCUBAS}} - V_{\text{obs}}}{V_{\text{obs}}} \times 100\%\right)$, quantifies the systematic directional bias of the model, that is, whether SCUBAS tends to over- or underpredict the observed voltages. The median absolute error (MdAE), defined as $\text{MdAE} = \text{median}(|V_{\text{SCUBAS}} - V_{\text{obs}}|)$, provides the typical error magnitude in volts, offering a scale reference that is robust to extreme outliers. These metrics characterize the central tendency of the model–observation mismatch but do not assess model accuracy. The prediction efficiency (PE) calculated using the Nash–Sutcliffe Model Efficiency Coefficient (Nash & Sutcliffe, 1970), measures the fraction of observed variance explained by the model. A PE of 1.0 indicates perfect prediction; 0.0 means the model performs no better than predicting the observed mean at every time step; and negative values indicate performance worse than the mean. PE thus assesses whether the model predictions contain meaningful information about the observed signal variability beyond what would be captured by the time-series mean alone. MdPE and MdAE noted in the figure, are 22% and 222 V, which is considered acceptable, especially given the large measured voltage swing of ∼2,700 V at 02:02 UT. The PE is approximately 0.78, indicating strong agreement between the SCUBAS simulations and measured voltage variations during the event.

Figure 9 presents a quantitative comparison between SCUBAS model outputs and measured voltage fluctuations on the TAT-8 submarine cable during the March 1989 geomagnetic superstorm. The measured data were extracted from Figures 2 and 3 of Medford et al. (1989), which documented voltage responses on the cable to interplanetary (IP) shocks and subsequent geomagnetic activity. Specifically, Figure 2 in Medford et al. (1989) captures the IP shock arrival, characterized by a storm sudden commencement (SSC) and associated voltage spikes, while Figure 3 in Medford et al. (1989) shows magnetic field perturbations and voltage fluctuations throughout the storm's growth, main, and recovery phases. To digitize the historical voltage records (digital

magnetometer measurements were already available), a combination of machine learning-assisted extraction and manual correction was applied to ensure fidelity in the retrieved data sets (see supplementary documents). Figure 9a displays a one-hour data–model comparison during the SSC, focusing on the immediate voltage response to the IP shock's impact at the magnetopause. The model reproduces several key features of the observed response, including voltage spikes associated with interplanetary shocks, the dominant wave-like structures in the induced voltage, and much of the variability during the main phase of the storms. While some shorter-period fluctuations are less well resolved, the overall temporal evolution is captured reasonably well. During this interval, SCUBAS reproduces the peak induced voltage and the subsequent wave-like oscillations with good overall agreement in both timing and amplitude. The PE for this case is approximately 0.92, indicating excellent agreement. The improved model performance for the 1989 storm is likely due at least in part to the higher quality magnetometer input (no digitization of magnetograms required, more magnetometers near cable route).

Figure 9b extends the March 1989 comparison over a 24-hr period encompassing the storm's entire evolution. SCUBAS continues to capture the broad structure and amplitude of the voltage fluctuations, including the prominent negative-to-positive voltage swing between 01:00 and 02:00 UT on 14 March. The PE for this longer interval is approximately 0.83, resulting in an overall PE of approximately 0.85 for the entire storm event. It is important to note, however, that the model underperforms in capturing rapid high-frequency voltage variations observed between 21:00 and 23:00 UT on 13 March. While limited spatiotemporal resolution of the driving magnetometer data may contribute to this mismatch, additional factors are likely involved. These include the assumption of spatial coherence of the current structures along extended cable sections, frequency-dependent attenuation inherent in the layered transfer function, and the smoothing introduced by section-wise integration of the electric field. As a result, short-period, spatially localized disturbances may not be fully represented within the present modeling framework.

6. Discussion

This data–model comparison study, leveraging historically reported submarine cable voltage observations, was conducted to test the SCUBAS model's performance during extreme geomagnetic events, specifically the February 1958 and March 1989 superstorms. The results demonstrate that SCUBAS performs with high fidelity, achieving an overall PE of 0.85, with a peak PE of 0.92 and low PE of 0.78. The model accurately captures key features such as interplanetary shock-induced voltage spikes during both the storms; additionally, it captures the dominant voltage swings during the main phase of the March 1989 storm, including the large negative-to-positive excursion between 01:30 and 02:30 UT on 14 March, while underperforming in reproducing the rapid wave-like variations observed between 2100 and 2300 UT on 13 March. Contemporary reports of the February 1958 storm describe rapid changes in transatlantic radio communication weakening and then briefly become much stronger, during the main disturbance interval (Brooks, 1959). This behavior is broadly consistent with strongly time, varying ionospheric conditions (e.g., high-frequency absorption and other impacts on skywave propagation) expected under intense auroral forcing. The oscillatory signatures in the ESK H component and the corresponding modeled response occur on similar timescales, which may suggest a shared "storm-time variability" backdrop rather than a one-to-one causal connection. We therefore cite Brooks (1959) as qualitative context for the rapid variability during this interval, without treating it as an indirect validation of broad scale features in the observations.

Further, the temporal development of the February 1958 storm appears qualitatively different from that of March 1989. As documented by Hakura and Nagai (1964), the 1958 event followed relatively quiet conditions until two sharp sudden commencements at 01:26 and 01:59 UT on 11 February initiated intense polar and auroral disturbances. The three-hour A_p index rose rapidly to ∼400 nT early in the event, whereas in March 1989 similar A_p levels were reached later, after sustained ring current growth had already driven D_{st} to its minimum of −586 nT (A_p time series provided in the Supplementary Material). AE reached ∼2,500 nT in February 1958 storm during the same time of largest voltage excursions in TAT-1 cable, compared to ∼1,800 nT in 1989, suggesting considerably stronger auroral electrojet activity during the earlier event (refer to Figure 5). Additionally, geomagnetic latitude contours overlaid on Figure 1 show that TAT-1 was located at a higher MLAT position than TAT-8, placing it closer to the auroral forcing region. This combination of rapid onset and enhanced high-latitude current systems in 1958 may help explain the larger voltage excursions observed on TAT-1 despite the more extreme D_{st} minimum in March 1989.

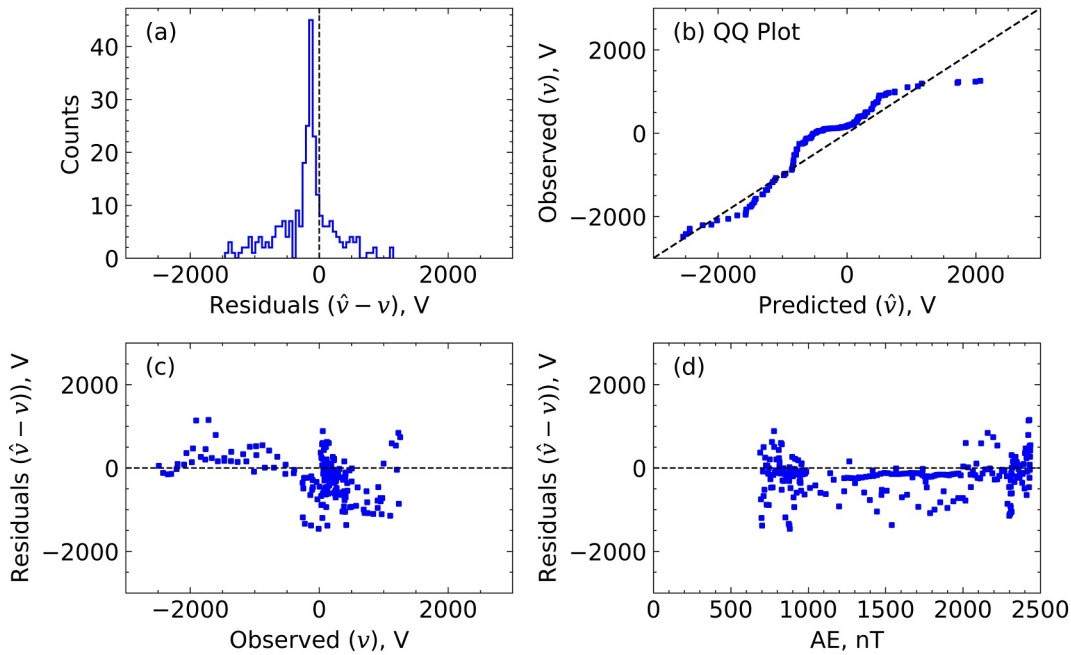

Figure 10. Error/residual ($\hat{v} - v$) analysis of the data-model comparison for February 1958 storm event showing, (a) distribution of residuals, (b) quantile-quantile plots of predicted versus observed, (c) residuals as a function of observed, and (d) residuals as a function of AE.

Additional important insight from this analysis is that the geomagnetically induced voltage during the February 1958 storm on the TAT-1 cable was nearly four times larger than that recorded on the TAT-8 cable during the March 1989 storm—despite the latter being associated with higher geomagnetic activity based on global indices (minimum Dst −569 nT). A likely contributing factor is the differing ocean depths along the two cable routes and geomagnetic latitudes, both of which directly influence the transfer function amplitude and the spatial coherence of the driving magnetic perturbations, respectively, as discussed in Boteler et al., 2023. Within the SCUBAS framework, these effects are explicitly calculable through route-dependent conductivity structure and magnetic forcing; a dedicated sensitivity experiment isolating MLAT and bathymetry effects is left for follow-on work. These findings align with prior GIC impact research (e.g., Pulkkinen et al., 2017), which highlights that extreme geomagnetic storms do not always translate to proportionally extreme impacts on critical infrastructure. To further evaluate the model's accuracy and potential biases, we conducted a detailed error analysis using the data sets from both superstorm events. This analysis reinforces SCUBAS's reliability across various storm phases and identifies areas for refinement in future model development and implementation.

To quantitatively assess the model performance discussed above, we now examine the residual diagnostics for both events. Figure 10 presents a detailed error/residual analysis evaluating the performance of the SCUBAS model by comparing simulated and measured voltage fluctuations on the TAT-1 submarine cable during the February 1958 geomagnetic superstorm. Note in this case residuals are simply difference between prediction ($\hat{v}$) and observed (v) voltages. The analysis focuses on the initial phase of the storm, incorporating a 3.5-hr data segment between 01:00 and 04:00 UT on 11 February 1958. The largest residuals in panel (c) are associated with the rapid voltage excursion near 02:02 UT, where the observed voltage swings from approximately −2,700 to +1,000 V within a short time interval. Outside this interval, residuals remain comparatively small. Panel (d) reveals no systematic trend in the residuals with respect to AE values, suggesting that the model's reduced accuracy is primarily associated with periods of rapid voltage fluctuation rather than the absolute intensity of the global geomagnetic activity level. Rather than being related to SCUBAS model performance, at least some of these errors are related to the digitization of the magnetograms, the voltages, or both. In particular, large voltage or magnetic field fluctuations may be difficult to capture accurately via the digitization processing as they are very difficult to view by human eye or ML algorithms for that matter.

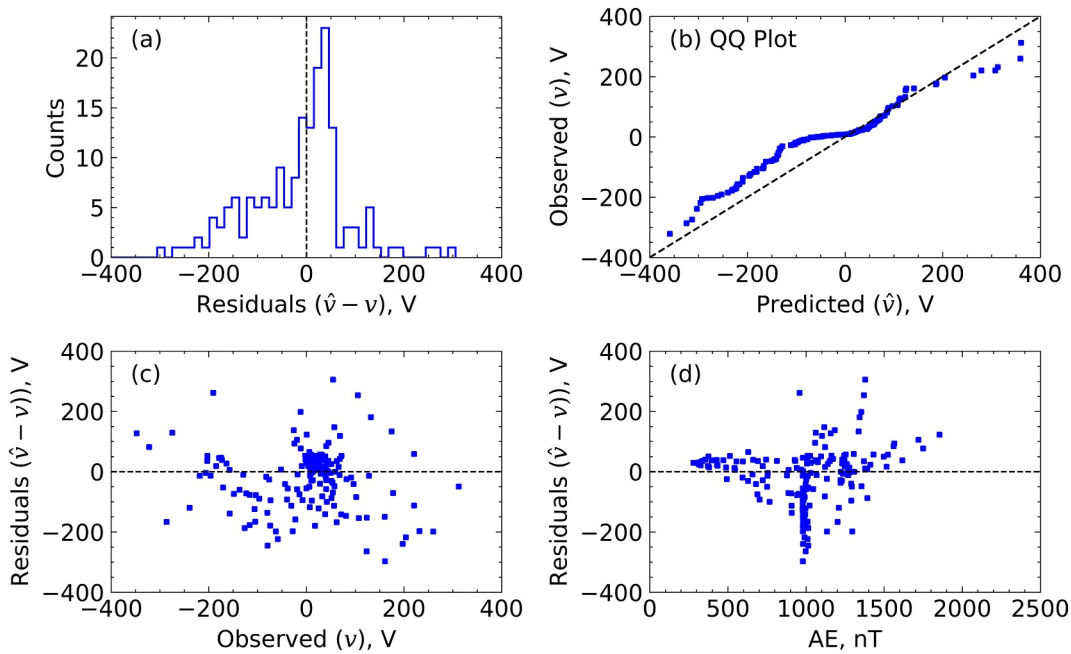

Figure 11. Error analysis of the data-model comparison for March 1989 storm event showing, (a) distribution of residuals, (b) quantile-quantile plots of predicted versus observed, (c) residual as a function of observed, and (d) residual as a function of AE.

Figure 11 presents a detailed error analysis of the SCUBAS model performance by comparing simulated and measured voltage fluctuations during the March 1989 geomagnetic superstorm. This analysis incorporates data from both the SSC and the subsequent main phase of the event. The residual distribution (panel a) shows that the residuals are approximately centered about zero, though a modest negative skew is present, reflecting intervals where the model underpredicts the observed voltage. The Q–Q plot (panel b) deviates from the y = x line, particularly in the negative range, further indicating this asymmetry. Compared to the 1958 event (Figure 10a–note the different x-axis range), the 1989 residual distribution is more symmetric and tightly concentrated, consistent with the improved magnetometer coverage available for the TAT-8 cable route — three stations (FRD, STJ, HAD) distributed along the route versus a single station (ESK) for TAT-1. This suggests that model deviations are not systematically biased over the analyzed interval, although localized discrepancies remain. Panel c shows that the residuals are evenly distributed with respect to measured voltages, implying that the model does not exhibit systematic bias across voltage amplitudes. Panel (d) shows no statistically significant trend in residuals with AE. However, a cluster of large residuals is evident around AE ∼1,000 nT, corresponding to the main phase interval between 20 UT on 13 March and 0 UT on 14 March, when the model underpredicts the observed voltage.

While SCUBAS demonstrates strong overall performance, particularly under moderate geomagnetic activity, our findings suggest areas for improvement—especially during the peak phases of intense storms. One key limitation arises from the absence of small-scale ionospheric and magnetospheric current structures, which can result from nonlinear coupling processes and are not reflected in the input data due to lack of sufficient ground magnetometer measurements needed to capture GMD from the small-scale currents (Boteler et al., 2024). Because such fine-scale currents decorrelate over relatively short spatial scales, SCUBAS does not interpolate or reconstruct unresolved magnetic structure across long cable routes. As a result, the model captures large-scale voltage envelopes effectively, but localized or rapidly varying current systems may contribute to discrepancies at shorter temporal and spatial scales. Additionally, the reliance on interpolation techniques to compensate for sparse historical magnetometer data—particularly the lack of ocean-based observations—likely contributes to the model's reduced accuracy during periods of elevated geomagnetic disturbance, as outlined in Tables 3 and 4. This factor may also have caused the lower PE during the 1958 storm, as there were no magnetometers near the western end of the TAT-1 cable (Figure 1), in contrast to the TAT-8 cable in the 1989 storm. Both TAT-1 and TAT-8 cables span approximately 4,000 and 6,500 km, respectively, across the Atlantic Ocean, covering up to five hours of magnetic local time. Consequently, because different cable segments are excited by magnetic observations from different

geomagnetic stations (see Tables 1 and 2), and are underlain by varying conductivity structures and ocean depths, segments along the same cable may experience substantially different magnetic field variations and corresponding induced voltages. No spatial interpolation of magnetic perturbations is performed, as storm-time magnetic structures can decorrelate over regional scales. This spatial variability can lead to scenarios in which induced electric fields in adjacent cable sections are oppositely directed, resulting in partial or full cancellation of net voltage. This phenomenon has been noted in prior studies, including Boteler et al. (2024) and Lanzerotti et al. (2001). Enhancing the SCUBAS model by incorporating higher-resolution spatiotemporal magnetometer data sets and improved Earth conductivity profiles would help address these limitations. Such refinements will be a focus on future development efforts aimed at improving model fidelity during the most geomagnetically active periods.

7. Challenges in Modeling Underwater Geomagnetically Induced Currents (GICs)

Modeling GICs in submarine environments presents significant scientific and logistical challenges. A primary limitation arises from sparse geomagnetic sampling over oceanic regions, where submarine cables are often routed far from land-based observatories. Consequently, magnetic forcing along much of the cable must be inferred from distant stations, introducing spatial uncertainty. Although limited seabed magnetic observations exist in research settings (e.g., Ocean Networks Canada), offshore coverage remains far less dense than terrestrial geomagnetic networks.

Additionally, the proprietary nature of submarine cable data sets further complicates the validation process. Voltage and current measurements from undersea cables are held by private telecommunications and infrastructure companies and are generally not accessible to the scientific community. This restricts opportunities for direct comparison between model outputs and observed data, hindering comprehensive validation.

For this study, an added layer of complexity was the reliance on historical data sets. Many magnetometer records from February 1958 and March 1989 geomagnetic superstorms were recorded in analog format. Digitizing these magnetograms was a necessary but non-trivial step, as the reconstructed magnetic time series form the primary input to the induction calculations. While SCUBAS is primarily sensitive to storm-scale and mesoscale geomagnetic variability rather than very short-period fluctuations, preserving the overall amplitude envelope and major temporal gradients was important for reliable voltage estimation. The quality and legibility of the original magnetograms varied considerably, and in some cases degradation of the physical records limited our ability to recover fully consistent digital traces. This uncertainty may have contributed to discrepancies during intervals of rapid magnetic variability. In several intervals, particularly during rapid or large-amplitude excursions, portions of the original magnetogram traces are visually ambiguous due to image degradation and contrast limitations. In these cases, both automated extraction and manual verification introduce measurable uncertainty in the reconstructed time series. These limitations are inherent to the quality of the archival records rather than to the modeling framework itself.

Because SCUBAS is based on the DSTL formulation of thin-sheet approximation, thus the model response is inherently governed by (a) the integrated conductance of the seawater and sediment layers, and (b) the spatial gradients in the imposed geomagnetic perturbations. Consequently, the spatial and temporal scales resolved by the model depend on the segmentation length relative to the adjustment distance, the width and depth of oceanic features (i.e., continental shelves vs. deep ocean), and the spatial variability of the input magnetic observatory data. These dependencies have been examined in detail in recent study by Boteler et al. (2023), which explicitly demonstrate how conductance and spatial variability in geomagnetic forcing control the induced electric fields and currents. The present formulation is therefore consistent with, and builds upon, these established results. For the March 1989 event, the use of multiple geomagnetic stations distributed across the North Atlantic avoids imposing artificial spatial uniformity along the ~8,000 km cable. The H-component time series from different stations are not identical and become weakly correlated during portions of the main phase, indicating structured and evolving overhead current systems. Mapping these spatially varying perturbations into distributed GEFs is therefore physically more realistic than enforcing a single-station solution.

Despite these significant limitations, this study successfully assembled and processed key historical data sets through cross-disciplinary collaboration among experts in magnetometry, data science, and geophysics. While data scarcity inevitably affects the precision of model outputs, the effort underscores the importance of integrating archival data, innovative digitization techniques, and community cooperation to advance modeling capabilities

for GIC impacts under the water. In future we plan to establish sustained collaborations between cable operators (e.g., Australia Japan Cable Network, Google, Meta) and the scientific community to enable validation of SCUBAS against recent geomagnetic storm events using observations in modern cables and ground magnetometer networks. Such partnerships will provide the necessary data fidelity to evaluate model performance and improve confidence in submarine cable GIC forecasting.

8. Conclusions

This study presents the first data–model validation of SCUBAS by comparing simulated and observed underwater voltage fluctuations during two of the most intense geomagnetic superstorms of the 20th century: the February 1958 and March 1989 events. Both storms were severe enough to disrupt critical infrastructure and impact human activity across the North Atlantic sector. Using historical data sets reported in the literature, we validated SCUBAS model outputs against measured voltage measurements along the TAT-1 and TAT-8 submarine cables. The simulation results demonstrate that SCUBAS captures the essential features of the storm-driven induced electric fields with high fidelity. Across most phases of the storms, the model shows strong overall agreement with the observations, with an average PE of 0.85. This suggests that SCUBAS captures the bulk storm-time voltage response, particularly at larger spatiotemporal scales. While the model performs consistently using available inputs, its accuracy is expected to improve with denser spatial coverage of ground magnetometers along the cable route and improved constraints on subsurface conductivity structure. This validation effort strengthens confidence in the SCUBAS model as a reliable first-principles tool for assessing space weather impacts on submarine cables. It lays a critical foundation for future studies on extreme event simulations, infrastructure vulnerability assessments, and geoelectric hazard forecasting.

Conflict of Interest

The authors declare no conflicts of interest relevant to this study.

Availability Statement

The crust and lithospheric model of the Earth LITHO1.0 model (Pasyanos et al., 2014) is available on IRIS DMC Data Products website (Trabant et al., 2012). The computational model, SCUBAS: Submarine Cables Upset by Auroral Streams., is developed using Python to compute geomagnetic induction effect on submarine cables (Chakraborty et al., 2022). A pip installer is also available to install the model in any python environment. Example codes are also available to describe the parameters and illustrate the use of SCUBAS (Chakraborty et al., 2022). Please refer to the website for detailed documentation on SCUBAS. The majority of analysis and visualization was completed with the help of free, open-source software tools such as matplotlib (Hunter, 2007), IPython (Perez & Granger, 2007), pandas (McKinney, 2010), and others (e.g., Millman & Aivazis, 2011). Our code, data sets, magnetograms, digitized data sets are published in Zenodo repository (Chakraborty, 2025).

Acknowledgments

SC, MDH, and XS are supported by NSF GEM 2452540 and 2402336, and NASA award 80NSSC24K1026. SC is also supported by Center for Space and Atmospheric Research at ERAU. DHB was supported by Natural Resources Canada. The magnetic observatory data for the February 1958 and March 1989 storms are available from the respective observatory operators: Fredericksburg—United States Geological Survey, St Johns—Natural Resources Canada, Eskdalemuir and Hartland—British Geological Survey, or from the World Data Centre for Geomagnetism, Kyoto. NRCan contribution number: 20220386. Authors acknowledge and thank Dr. E. Joshua Rigler from U.S. Geological Survey Geomagnetism Program (USGS) for his valuable inputs and sharing the historical magnetograms from USGS archives.

References

Akasofu, S.-I., & Chapman, S. (1963). The lower limit of latitude (US sector) of northern quiet auroral arcs, and its relation to Dst(H). *Journal of Atmospheric and Terrestrial Physics*, *25*(1), 9–12. https://doi.org/10.1016/0021-9169(63)90011-4

Amante, C., & Eakins, B. W. (2009). *ETOPO1 1 arc-minute global relief model: Procedures, data sources and analysis*. NOAA Technical Memorandum NESDIS NGDC-24. Retrieved from https://www.ngdc.noaa.gov/mgg/global/relief/E

Anderson, C. W. (1978). Magnetic storms and cable communications. In C. F. Kennel, L. J. Lanzerotti, & E. N. Parker (Eds.), *Solar system plasma physics*. North-Holland.

Anderson, C. W., III., Lanzerotti, L. J., & Maclennan, C. G. (1974). Outage of the L4 system and the geomagnetic disturbances of 4 August 1972. *Bell System Technical Journal*, *53*(9), 1817–1837. https://doi.org/10.1002/j.1538-7305.1974.tb02817.x

Ash, S. (2016). The history of the repeater. *History of the Atlantic Cable & Undersea Communications From the First Submarine Cable of 1850 to the Worldwide Fiber Optic Network*. Retrieved from https://atlantic-cable.com/Article/SA/65/index.htm

Axe, G. A. (1968). Effects of earths magnetism on submarine cables. *Post Office Electrical Engineers' Journal*, *61*, 37. https://www.worldradiohistory.com/UK/POEEJ/60s/Post-Office-Electrical-Engineers-Journal-1968-04.pdf

Barlow, W. H., & Culley, R. S. (1849). VI. On the spontaneous electrical currents observed in the wires of the electric telegraph. *Philosophical Transactions of the Royal Society of London*, 61–72. https://doi.org/10.1098/rstl.1849.0006

Beggan, C. D., Clarke, E., Lawrence, E., Eaton, E., Williamson, J., Matsumoto, K., & Hayakawa, H. (2024). Digitized continuous magnetic recordings for the August/September 1859 storms from London, UK. *Space Weather*, *22*(3), e2023SW003807. https://doi.org/10.1029/2023SW003807

Boteler, D. H. (2006). The super storms of August/September 1859 and their effects on the telegraph system. *Advances in Space Research*, *38*(2), 159–172. https://doi.org/10.1016/j.asr.2006.01.013

Boteler, D. H. (2019). A 21st century view of the March 1989 magnetic storm. *Space Weather*, *17*(10), 1427–1441. https://doi.org/10.1029/2019sw002278

Boteler, D. H., Chakraborty, S., Shi, X., Hartinger, M. D., & Wang, X. (2023). Transmission line modelling of geomagnetic induction in the Ocean/Earth conductivity structure. *International Journal of Geosciences*, *14*(8), 767–791. https://doi.org/10.4236/ijg.2023.148041

Boteler, D. H., Chakraborty, S., Shi, X., Hartinger, M. D., & Wang, X. (2024). An examination of geomagnetic induction in submarine cables. *Space Weather*, *22*(2), e2023SW003687. https://doi.org/10.1029/2023SW003687

Brooks, J. (1959). A reporter at large: The subtle storm. *The New Yorker*. https://www.newyorker.com/magazine/1959/02/07/the-subtle-storm

Carter, L., Burnett, D., Drew, S., Hagadorn, L., Marle, G., Bartlett-Mcneil, D., et al. (2009). *Submarine cables and the oceans – Connecting the world*. UNEP-WCMC Biodiversity.

Chakraborty, S. (2025). Legacy storm analysis. *Zenodo*. https://doi.org/10.5281/zenodo.17653406

Chakraborty, S., Boteler, D. H., Shi, X., Murphy, B. S., Hartinger, M. D., Wang, X., et al. (2022). Modeling geomagnetic induction in submarine cables. *Frontiers in Physics*, *10*, 1022475. https://doi.org/10.3389/fphy.2022.1022475

Cid, C., Palacios, J., Saiz, E., Guerrero, A., & Cerrato, Y. (2014). On extreme geomagnetic storms. *Journal of Space Weather and Space Climate*, *4*, A28. https://doi.org/10.1051/swsc/2014026

Gil, A., Berendt-Marchel, M., Modzelewska, R., Moskwa, S., Siluszyk, A., Siluszyk, M., et al. (2021). Evaluating the relationship between strong geomagnetic storms and electric grid failures in Poland using the geoelectric field as a GIC proxy. *Journal of Space Weather and Space Climate*, *11*, 30. https://doi.org/10.1051/swsc/2021013

Hakura, Y., & Nagai, M. (1964). Synthetic study of severe solar-terrestrial disturbances on February 9 12, 1958. *Journal of the Radio Research Laboratories*, *11*(56, July), 197–250.

Hayakawa, H., Ebihara, Y., & Hata, H. (2023). A review for Japanese auroral records on the three extreme space weather events around the International Geophysical Year (1957–1958). *Geoscience Data Journal*, *10*(1), 142–157. https://doi.org/10.1002/gdj3.140

Hunter, J. D. (2007). Matplotlib: A 2D graphics environment. *Computer Science and Engineering*, *9*(3), 90–95. https://doi.org/10.1109/MCSE.2007.55

Kataoka, R., & Kazama, S. (2019). A watercolor painting of northern lights seen above Japan on 11 February 1958. *Journal of Space Weather and Space Climate*, *9*, A28. https://doi.org/10.1051/swsc/2019027

Kataoka, R., Uchino, S., Fujiwara, Y., Fujita, S., & Yamamoto, K. (2019). Fan-shaped aurora as seen from Japan during a great magnetic storm on February 11, 1958. *Journal of Space Weather and Space Climate*, *9*, A16. https://doi.org/10.1051/swsc/2019013

Lanzerotti, L. J. (2007). Space weather effects on communications. In *Space weather-physics and effects* (pp. 247–268). Springer.

Lanzerotti, L. J. (2017). Space weather: Historical and contemporary perspectives. *Space Science Reviews*, *212*(3), 1253–1270. https://doi.org/10.1007/s11214-017-0408-y

Lanzerotti, L. J., Medford, L. V., Maclennan, C. G., Kraus, J. S., Kappenman, J., & Radasky, W. (2001). Trans-Atlantic geopotentials during the July 2000 solar event and geomagnetic storm. *Solar Physics*, *204*(1/2), 351–359. https://doi.org/10.1023/a:1014289410205

Marti, L., Yiu, C., Rezaei-Zare, A., & Boteler, D. (2014). Simulation of geomagnetically induced currents with piecewise layered-Earth models. *IEEE Transactions on Power Delivery*, *29*(4), 1886–1893. https://doi.org/10.1109/tpwrd.2014.2317851

McKinney, W. (2010). Data structures for statistical computing in Python. In S. van der Walt & J. Millman (Eds.), *Proceedings of the 9th Python in science conference* (pp. 56–61). https://doi.org/10.25080/Majora-92bf1922-012

McManus, D. J., Carr, H. H., & Adams, B. M. (2011). Global telecommunications security: Effects of geomagnetic disturbances. *International Journal of Interactive Mobile Technologies*, *5*(3), 6. https://doi.org/10.3991/ijim.v5i3.1667

Medford, L. V., Lanzerotti, L. J., Kraus, J. S., & Maclennan, C. G. (1989). Transatlantic earth potential variations during the March 1989 magnetic storms. *Geophysical Research Letters*, *16*(10), 1145–1148. https://doi.org/10.1029/gl016i010p01145

Millman, K. J., & Aivazis, M. (2011). Python for scientists and engineers. *Computer Science and Engineering*, *13*(2), 9–12. https://doi.org/10.1109/MCSE.2011.36

Nash, J. E., & Sutcliffe, J. V. (1970). River flow forecasting through conceptual models part I — A discussion of principles. *Journal of Hydrology*, *10*(3), 282–290. https://doi.org/10.1016/0022-1694(70)90255-6

North American Electric Reliability Corporation (NERC). (2022). *GMD event data download guide*. NERC. Retrieved from https://www.nerc.com/pa/RAPA/GMD/Documents/GMD_Event_Data_Download_Guide_May_2022.pdf

Ohtani, S., Odagi, Y., Matsuoka, A., & Iyemori, T. (2024). Dayside magnetic depression following interplanetary shock arrivals during the February 1958 and July 1959 superstorms. *Space Weather*, *22*(10), e2024SW004017. https://doi.org/10.1029/2024SW004017

Pasyanos, M. E., Masters, T. G., Laske, G., & Ma, Z. (2014). Litho1.0: An updated crust and lithospheric model of the earth. *Journal of Geophysical Research: Solid Earth*, *119*(3), 2153–2173. https://doi.org/10.1002/2013JB010626

Perez, F., & Granger, B. E. (2007). Ipython: A system for interactive scientific computing. *Computer Science and Engineering*, *9*(3), 21–29. https://doi.org/10.1109/MCSE.2007.53

Prescott, G. B. (1866). History, theory and practice of the electric telegraph. *Ticknor and Fields*.

Pulkkinen, A., Bernabeu, E., Thomson, A., Viljanen, A., Pirjola, R., Boteler, D., et al. (2017). Geomagnetically induced currents: Science, engineering, and applications readiness. *Space Weather*, *15*(7), 828–856. https://doi.org/10.1002/2016SW001501

Rohatgi, A. (n.d.). WebPlotDigitizer (Version 5.2). Retrieved from https://automeris.io

Trabant, C., Hutko, A. R., Bahavar, M., Karstens, R., Ahern, T., & Aster, R. (2012). Data products at the IRIS DMC: Stepping stones for research and other applications. *Seismological Research Letters*, *83*(5), 846–854. https://doi.org/10.1785/0220120032

Winckler, J. R., Peterson, L., Hoffman, R., & Arnoldy, R. (1959). Auroral X-rays, cosmic rays, and related phenomena during the storm of Feb 10-11, 1958. *Journal of Geophysical Research*, *64*(6), 597–610. https://doi.org/10.1029/jz064i006p00597